ESC European Society of Cardiology

Cardiovascular Research (2023) **119**, 221–235
https://doi.org/10.1093/cvr/cvac077

Ryanodine receptor 2 (RYR2) dysfunction activates the unfolded protein response and perturbs cardiomyocyte maturation

Yuxuan Guo [1,2,3,4]*†, Yangpo Cao[5†], Blake D. Jardin[5†], Xiaoran Zhang [5], Pingzhu Zhou[5], Silvia Guatimosim [6], Junsen Lin[1,2,3,4], Zhan Chen[1,2,3,4], Yueyang Zhang[1,2,3,4], Neil Mazumdar[5], Fujian Lu[5], Qing Ma [5], Yao-Wei Lu [5], Mingming Zhao[3,4,7,8], Da-Zhi Wang[5], Erdan Dong[2,3,4,7,8], and William T. Pu[5,9]*

[1]Peking University Health Science Center, School of Basic Medical Sciences, Beijing 100191, China; [2]Institute of Cardiovascular Sciences, Peking University, Beijing 100191, China; [3]Key Laboratory of Molecular Cardiovascular Science, Ministry of Education, Beijing 100191, China; [4]Beijing Key Laboratory of Cardiovascular Receptors Research, Beijing 100191, China; [5]Department of Cardiology, Boston Children's Hospital, 300 Longwood Ave, Boston, MA 02115, USA; [6]Department of Physiology and Biophysics, Institute of Biological Sciences, Universidade Federal de Minas Gerais, Av. Antônio Carlos 6627, Belo Horizonte MG - CEP 31270-901, Brazil; [7]Department of Cardiology and Institute of Vascular Medicine, Peking University Third Hospital, Beijing 100191, China; [8]NHC Key Laboratory of Cardiovascular Molecular Biology and Regulatory Peptides, Beijing 100191, China; and [9]Harvard Stem Cell Institute, 7 Divinity Avenue, Cambridge, MA 02138, USA

Received 21 August 2021; revised 3 April 2022; accepted 5 May 2022; online publish-ahead-of-print 16 May 2022

Aims Calcium-handling capacity is a major gauge of cardiomyocyte maturity. Ryanodine receptor 2 (RYR2) is the pre-dominant calcium channel that releases calcium from the sarcoplasmic reticulum/endoplasmic reticulum (SR/ER) to activate cardiomyocyte contraction. Although RYR2 was previously implied as a key regulator of cardiomyocyte maturation, the mechanisms remain unclear. The aim of this study is to solve this problem.

Methods and results We performed Cas9/AAV9-mediated somatic mutagenesis to knockout RYR2 specifically in cardiomyocytes in mice. We conducted a genetic mosaic analysis to dissect the cell-autonomous function of RYR2 during cardiomyocyte maturation. We found that RYR2 depletion triggered ultrastructural and transcriptomic defects relevant to cardiomyocyte maturation. These phenotypes were associated with the drastic activation of ER stress pathways. The ER stress alleviator tauroursodeoxycholic acid partially rescued the defects in RYR2-depleted cardiomyocytes. Overexpression of ATF4, a key ER stress transcription factor, recapitulated defects in RYR2-depleted cells. Integrative analysis of RNA-Seq and bioChIP-Seq data revealed that protein biosynthesis-related genes are the major direct downstream targets of ATF4.

Conclusion RYR2-regulated ER homeostasis is essential for cardiomyocyte maturation. Severe ER stress perturbs cardiomyocyte maturation primarily through ATF4 activation. The major downstream effector genes of ATF4 are related to protein biosynthesis.

* Corresponding authors. E-mail: guo@bjmu.edu.cn (Y.G.); E-mail: william.pu@cardio.chboston.org (W.T.P.)
† These authors contributed equally to this work.

Graphical Abstract

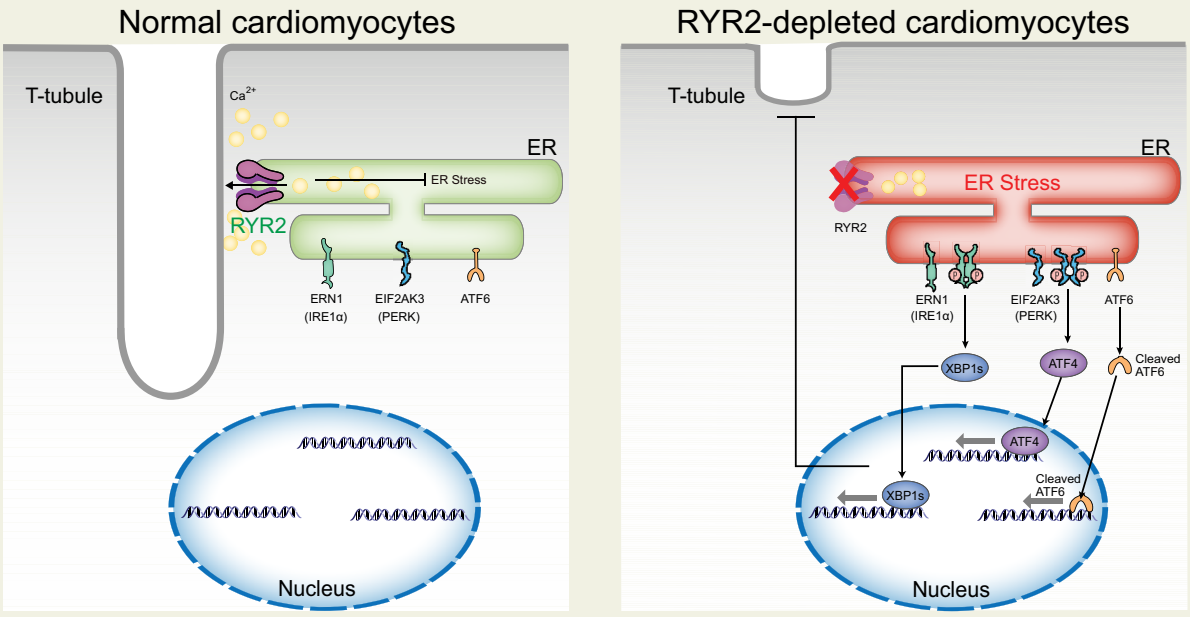

RYR2 dysfunction activates ER stress and perturbs T-tubule maturation.

Keywords Cardiomyocyte maturation • Ryanodine receptor 2 • ER stress

1. Introduction

Cardiomyocyte maturation is a critical developmental step for cardiomyocytes to obtain the myriad specializations necessary to fulfill the needs of the post-natal mammalian circulation.[1–3] Cardiomyocyte maturation is closely associated with cell cycle withdrawal and loss of cardiac regenerative capacity. The inability of stem cell-derived cardiomyocytes to fully mature is a major bottleneck in cardiac regenerative medicine. Perturbations in cardiomyocyte maturation could also cause cardiomyopathy. Thus, investigating the mechanisms that control cardiomyocyte maturation is important for understanding cardiac pathophysiology and developing novel disease therapies.

Mature cardiomyocytes harness elaborate mechanisms to support efficient, coordinated excitation–contraction coupling. During cardiomyocyte contraction, the depolarization of the plasma membrane activates L-type calcium channels (LTCCs) and induces a small influx of calcium into specialized cytoplasmic nanodomains called dyads. This calcium influx activates ryanodine receptor 2 (RYR2), the major calcium channel on the sarcoplasmic reticulum (SR), which is the specialized endoplasmic reticulum (ER) in cardiomyocytes. Activated RYR2 rapidly releases a large amount of calcium from the SR lumen into the cytoplasm. This RYR2-mediated calcium release leads to a sharp increase of cytoplasmic calcium concentration, which activates the myofibrils to drive cellular contraction.[4,5]

In development, the maturation of calcium-handling capacity is achieved through the increase of key calcium-handling proteins, such as LTCC and RYR2. In addition, the plasma membrane invaginates into the cell interior to form transverse tubules (T-tubules).[6,7] T-tubules facilitate action potential propagation from the cell surface to interior, thereby coordinating rapid and synchronous calcium release throughout the intracellular space. Thus, T-tubule formation is an ultrastructural hallmark of mature excitation–contraction coupling and calcium handling in cardiomyocytes, which forms at the second and third week after birth in mice.

Although calcium-handling parameters are well-established readouts of cardiomyocyte maturation, very little is known about the roles of calcium in the regulation of cardiomyocyte maturation. The SR/ER lumen is the major calcium reservoir in cardiomyocytes. Perturbation of ER functions such as protein biogenesis, protein folding and post-translational modifications trigger the unfolded protein responses (UPRs) also referred to as ER stress.[8,9] Short-term, moderate ER stress is usually cell protective, but excessive, acute ER stress can damage cells and even trigger programmed cell death.

The contribution of ER stress to cardiac pathology, protection, and remodelling has been actively studied,[10,11] but whether ER stress regulates cardiomyocyte maturation is yet to be investigated. Despite the intriguing connection between calcium handling, ER homeostasis and cardiomyocyte maturation, dissecting the relationship between these processes has been technically challenging because the genetic manipulation of calcium-handling molecules in SR/ER, such as RYR2, often leads to acute cardiac dysfunction and animal death.[12] Probing the cell-autonomous functions of these molecules, without worrying about the confounding secondary effects of cardiac dysfunction, is particularly problematic.[13]

To circumvent these hurdles, we established the adeno-associated virus (AAV)-delivered CRISPR/Cas9-mediated somatic mutagenesis (CASAAV) technique.[14,15] CASAAV allows us to produce cardiac genetic mosaics to circumvent cardiac dysfunction and animal death phenotypes, providing an opportunity to investigate cell-autonomous gene functions *in vivo*. Using this tool, we previously generated RYR2 genetic mosaics in mice and discovered a novel role of RYR2 in T-tubule maturation.[14] Here, we further study the role of RYR2 in regulating ER homeostasis and cardiomyocyte maturation in mice.

2. Materials and methods

2.1 Animal

All animal strains and procedures were locally approved by the Institutional Animal Care and Use Committee of Boston Children's Hospital (reference number: 19-07-3969R) and the ethics review board of Peking University (reference number: LA2021034). All animal procedures conform to the current NIH guidelines for the Care and Use of Laboratory Animals. General anaesthesia was induced with 0.5–3% isoflurane in a flow chamber supplied with oxygen. *Rosa*$^{Cas9GFP/Cas9GFP}$ (Stock No.: 026175) and *Rosa*$^{BirA/BirA}$ (Stock No.: 010920) mice were obtained from the Jackson Laboratory.

2.2 Plasmids and AAV

We previously reported AAV-cTNT-Cre, AAV-sgRNA[Ryr2]-cTNT-Cre, and AAV-cTNT-GFP-version2 plasmids.[14,16] *Ryr2* knockout (KO) was achieved with sgRNAs 5′-tgaggtggttctgcagtgca-3′ and 5′-tgcttggcagcagaaggatt-3′. We synthesized a 3×HA-MCS-P2A fragment (Integrated DNA technologies, USA, gBlock) and inserted this fragment into the AAV-cTNT-GFP-version2 plasmid to produce the AAV-cTNT-3×HA-MCS-P2A-GFP vector (Addgene#175090). Next, we cloned *Atf4* (Dharmacon Inc, USA, MMM1013-202858570), *Xbp1s* (Dharmacon Inc, USA, MMM1013-202766393), *Atf6* (transOMIC, USA, TCM1004), and *Ddit3* (Dharmacon Inc, USA, MMM1013-202764200) coding sequences into the above vector to produce AAV-cTNT-3×HA-ATF4-P2A-GFP, AAV-cTNT-3×HA-XBP1s-P2A-GFP, AAV-cTNT-3×HA-ATF6N-P2A-GFP, and AAV-cTNT-3×HA-DDIT3-P2A-GFP plasmids. We also synthesized a bioHA fragment and used this fragment to modify the AAV-cTNT-3×HA-ATF4-P2A-GFP plasmid and produce AAV-cTNT-bioHA-ATF4-P2A-GFP.

We produced AAV9 as previously described.[17,18] In brief, 140 μg AAV-ITR, 140 μg AAV9-Rep/Cap, and 320 μg pHelper (pAd-deltaF6, Penn Vector Core) plasmids were produced by maxiprep (Invitrogen, USA, K210017) or Gigaprep (Invitrogen, USA, K210009XP), and triple transfected into HEK293T cells in ten 15-cm plates by polyethylenimine transfection reagent (Polysciences, USA, 23966-2). 60–72 h after transfection, cells were scraped off plates, resuspended in lysis buffer (20 mM Tris pH 8, 150 mM NaCl, 1 mM $MgCl_2$, 50 μg/mL Benzonase) and lysed by three freeze–thaw cycles. AAV in culture medium was precipitated by PEG8000 (VWR, USA, 97061-100), resuspended in lysis buffer, and pooled with cell lysates. AAV particles were next purified in a density gradient (Cosmo Bio USA, AXS-1114542) by ultracentrifugation (Beckman, USA, XL-90) with a VTi-50 rotor. The AAV was next concentrated in phosphate buffered saline (PBS) with 0.001% pluronic F68 (Invitrogen, USA, 24040032) using a 100 kD filter tube (Fisher Scientific, USA, UFC910024).

AAV titre was quantified by real-time PCR using a fragment of the cTNT promoter DNA to make a standard curve. PCR primers for AAV quantification were 5′-TCGGGATAAAAGCAGTCTGG-3′ and 5′-CCCAAGCTATTGTGTGGCCT-3′. SYBR Green master mix (Invitrogen, 4368577) was used in this quantification.

2.3 Echocardiography and electrocardiogram

Echocardiography was performed on a VisualSonics Vevo 2100 machine with Vevostrain software by an investigator blinded to genotype or treatment group. Animals were awake during this procedure and held in a standard handgrip.

The mice's Lead II electrocardiogram was measured with a Softron ECG processor and analyzed by SP2006 software (Softron Biotechnology, Beijing, China). The scientist who performed the measurements was blinded to the mouse group assignment. Five consecutive heartbeats were measured to calculate the average value for each animal.

2.4 *In situ* confocal imaging of myocardium

In situ myocardium imaging was performed following an established method.[19] In brief, isolated hearts were cannulated on a Langendorff apparatus, and perfused with perfusion buffer [10 mM HEPES (pH 7.4), 120.4 mM NaCl, 14.7 mM KCl, 0.6 mM KH_2PO_4, 0.6 mM Na_2HPO_4, 1.2 mM $MgSO_4$, 4.6 mM $NaHCO_3$, 30 mM Taurine, 10 mM 2,3-butanedione monoxime (BDM), 5.5 mM glucose] at room temperature for 10 min. Where indicated, FM 4-64 (Invitrogen, USA, 13320) and Hoechst 33342 (Invitrogen, USA) dyes were added to the perfusion buffer at 2 and 4 μg/mL, respectively. After perfusion, the hearts were positioned on a glass-bottom dish, and immediately imaged using an inverted confocal microscope (Olympus FV3000RS).

2.5 Cardiomyocyte isolation

Cardiomyocytes were isolated by retrograde collagenase-II perfusion.[20] In brief, heparin-pre-treated mice were anaesthetized in a chamber with 0.5–3% isoflurane titrated to effect. Hearts were isolated and cannulated onto a Langendorff perfusion apparatus. 37°C perfusion buffer [10 mM HEPES (pH 7.4), 120.4 mM NaCl, 14.7 mM KCl, 0.6 mM KH_2PO_4, 0.6 mM Na_2HPO_4, 1.2 mM $MgSO_4$, 4.6 mM $NaHCO_3$, 30 mM Taurine, 10 mM BDM, 5.5 mM glucose] was first pumped into the heart to flush out blood and equilibrate the heart. 2 mg/mL Collagenase II (Worthington, USA, LS004177) was next perfused into the heart for 10 min at 37°C to dissociate cardiomyocytes. The apex was cut from the digested heart, gently dissociated into single cardiomyocytes in 10% foetal bovine serum/perfusion buffer and filtered through a 100 μm cell strainer to remove undigested tissues.

2.6 Contractility measurement and calcium imaging

Calcium was re-introduced into isolated cardiomyocytes by treating cells with a series of 5 mL perfusion buffers containing 100 μM, 400 μM, 900 μM, and 1.2 mM $CaCl_2$. At each step, cardiomyocytes were allowed to sediment for 5 min at room temperature before cells were transferred to the next buffer with a higher calcium concentration.[16]

In calcium imaging, the cardiomyocytes were loaded with 5 μM Rhod-2 for 10 min, washed with normal Tyrode solution (140 mM NaCl, 4 mM KCl, 1 mM $MgCl_2$, 1.8 mM $CaCl_2$, 10 mM glucose, 5 mM HEPES, pH 7.4, adjusted with NaOH) and next settled in a laminin-coated glass-bottom flow chamber at 30°C. The cells were electrically stimulated at 1 Hz to produce steady-state conditions. Calcium signals were next acquired through confocal line scanning using a ×60 objective. The line scan was positioned along the long axis of the cell in the cytosol, avoiding the nuclear area. The calcium signal was quantified manually using ImageJ.[16]

For the contractility assay, cardiomyocytes were plated on laminin-coated coverslips in media with 10 mM BDM and incubated for 30 min at 37°C and 5% CO_2. The coverslips were then transferred into a 37°C flow chamber with 1.2 μM $CaCl_2$ perfusion buffer without BDM. Cardiomyocytes were electrically stimulated at 1 Hz and cell

contraction was measured using an IonOptix system and a ×40 objective. Contractile and non-contractile cardiomyocytes were identified visually.[16]

2.7 Fluorescence imaging and analysis

Immunofluorescent labelling was performed as described.[21] Cardiomyocytes were first settled on laminin-coated glass coverslips for 30 min. Then, the cells were fixed with 4% paraformaldehyde for 10 min, permeabilized by 0.1% Triton-100/PBS for 10 min and blocked in 4% bovine serum albumin/PBS (blocking buffer) at 4°C overnight. Then, the cells were incubated with primary antibodies diluted in blocking buffer overnight at 4°C, washed with blocking buffer, and then incubated with secondary antibodies and dyes at room temperature for 2 h. The cells were next washed with PBS and mounted with ProLong Diamond antifade mountant (Invitrogen, 36961) before imaging. Antibodies and dyes are listed in Supplementary material online, *Table S3*.

For immunofluorescence on cryo-sections, hearts were harvested after isoflurane anaesthesia and fixed by 4% paraformaldehyde overnight at 4°C. Fixed hearts were cryoprotected by soaking in 15% sucrose followed by 30% sucrose at 4°C. Hearts were embedded in tissue-freezing medium (General Data, USA, TFM-5). 10 μm cryo-sections were cut using a cryostat (Thermo Scientific, USA, Microm HM 550). TdT-mediated dUTP nick end labelling (TUNEL) staining was performed using In Situ Cell Death Detection Kit (Roche Diagnostics, USA, # 11684795910) following manufacturer's instruction.

Confocal fluorescent images were taken using Olympus FV3000RS inverted laser scanning confocal microscope with a 60×/1.3 silicone-oil objective. Fluorescence intensity was measured using ImageJ. AutoTT[22] was used to quantify T-tubule and sarcomere organization. Cell size and shape were manually measured on maximally projected images.

2.8 Fluorescence-activated cell sorting

Isolated cardiomyocytes were filtered with a 100-μm cell strainer, pelleted by centrifugation at 20× *g* for 5 min and resuspended in ∼1 mL cold perfusion buffer. Fluorescence-activated cell sorting (FACS) was performed using a BD AriaII SORP cell sorter with a 100-μm nozzle.

2.9 RNA extraction and analysis

For real-time quantitative PCR (RT–qPCR) analysis using heart tissue, total RNA was purified using PureLink RNA Mini kit (Ambion, USA, 12183025). Genomic DNA removal and reverse transcription were performed using the QuantiTech reverse transcription kit (Qiagen, USA, 205311). Real-time PCR was performed using an ABI 7500 thermocycler.

For RT–qPCR using FACS-sorted cells, FACS was performed as described above. Samples were collected in a cooling device. Immediately after FACS, cells were centrifuged at 13 000 rpm at 4°C to remove supernatant. Total RNA was purified using PureLink RNA Micro kit (Thermo Fisher, USA, 12183016) and genomic DNA was removed by on-column DNase I digestion. Reverse transcription was performed using the SMART-Seq v4 Ultra Low Input RNA Kit (Clontech), which pre-amplified full-length cDNA before qPCR. Real-time PCR was performed using an ABI 7500 thermocycler.

RT–qPCR analysis of gene expression was performed by either Taqman quantification or SYBR reactions. The Taqman probes are as follow: Gapdh: 4352339E, Hspa5:Mm00517690_g1, Ddit3:Mm01135937_g1, Eif2ak3: Mm00438700_m1, Gapdh: Mm99999915_g1, Ern1: Mm00470233_m1, Atf6: Mm01295317_m1, Xbp1 (total): Mm00457357_m1 (Thermo Fisher Scientific). To specifically measure *Xbp1s* expression, we used 5′-GAGTCCGCAGCAGGTG-3′ and 5′-GTGTCAGAGTCCATGGGA-3′ primers for SYBR-based RTqPCR quantification (Invitrogen). As an internal control, we used 5′-AGGTCGGTGTGAACGGATTTG-3′ and 5′-TGTAGACCATGTAGTTGAGGTCA-3′ to measure *Gapdh*.

RT–PCR detection of *Xbp1s* splicing variants was performed using GoTaq PCR master mix (Promega, USA) and primers: 5′-ACACGCTTGGGAATGGACAC-3′ and 5′-CCATGGGAAGATGTTCTGGG-3′.

2.10 RNA-seq and data analysis

10 ng total RNA from FACS-isolated cardiomyocytes was reverse transcribed and full-length cDNA was specifically amplified by eight PCR cycles using SMART-Seq v4 Ultra Low Input RNA Kit (Clontech, USA).[23] RNA-seq libraries were constructed using Illumina's Nextera XT kit and single-end sequence reads were obtained using an Illumina NextSeq 500 sequencer.

RNA-seq reads were aligned to mm10 by STAR[24] and read counts were calculated by FeatureCounts .[25] DESeq2 was used to perform statistical analysis of differential gene expression.[26] An adjusted *P* value of 0.05 was used as the cutoff to identify differentially regulated genes. Gene ontology (GO) term analysis was performed using gene set enrichment analysis (GSEA) with ranked gene lists.[27] To visualize read distribution and Sashimi plots on genomic loci, bigwig files, generated by deeptools[28] with normalized read count, were loaded into the Integrative Genomics Viewer.[29]

2.11 Western blot analysis

Heart tissues were homogenized in RIPA buffer (25 mM Tris pH7.4, 150 mM NaCl, 1% Triton X-100, 0.5% Na Deoxycholate, 0.1% SDS) buffer supplemented with protease inhibitor cocktail at ∼33.3 mg/mL concentration. Heart lysates were denatured in 2× SDS sample buffer at 70°C for 10 min, separated on a 4–12% gradient gel (Invitrogen, USA, Bolt gels, NW04122BOX), transferred to a polyvinylidene difluoride membrane, and blocked by 4% milk/TBST. Primary antibodies were incubated with the membrane overnight at 4°C, followed by four 15-min TBST washes. Horseradish peroxidase (HRP)-conjugated secondary antibodies were probed for 1–2 h at room temperature, followed by four 15-min TBST washes. After adding Immobilon Western chemiluminescent HRP substrate (Millipore, USA, WBKLS0500), chemiluminescence was detected using a Li-Cor C-DiGit blot scanner. Antibodies used in this study are listed in Supplementary material online, *Table S3*.

2.12 bioChIP-seq and data analysis

For each biological replicate, four heart ventricles were collected from P28 *Rosa26*$^{birA/+}$ mice that were treated with AAV-bioHA-ATF4 at P1. The tissues were minced in 1% formaldehyde-containing PBS at room temperature by a motor-driven homogenizer (T10 basic. IKA). The tissue suspension was shaken for 15 min at room temperature for crosslinking. Next, glycine was added at a final concentration of 125 mM to quench formaldehyde. Chromatin isolation was performed as previously described.[30,31] A microtip sonicator (QSONICA Q700) was used at 60% amplitude and a cycle of 5 s on and 20 s off for 96 cycles in total. Sheared chromatin was pre-cleared by incubation with 100 μL Dynabeads Protein A (Life Technologies, USA, 10002D) for 1 h at 4°C. The pre-cleaned chromatin was then incubated with 100 μL Dynabeads M-280 Streptavidin (Life Technologies, USA, 11206D) for 1 h at 4°C. The streptavidin beads were washed and bound DNA eluted.

BioChIP DNA was purified with MinElute PCR Purification kit (Qiagen, USA, 28006). ChIP-seq libraries were constructed using a ChIP-seq library preparation kit (KAPA Biosystems, USA, KK8500). 50 ng of sonicated chromatin without pull-down was used as input.

Pair-end sequencing was performed on a NovaSeq sequencer. Reads were aligned to mm10 using Bowtie2[32] using default parameters. Peaks were called with MACS2[33] against input chromatin background. HOMER was used to annotate peaks to the nearest gene and to perform motif analysis (http://homer.ucsd.edu/homer/). DeepTools was used to generate aggregation and heatmap plots.[28] bioChIP-seq signal was visualized in the Integrated Genome Viewer.[29]

2.13 Statistical analysis

Statistical analysis and plotting were performed using JMP software (SAS Institute, USA) or GraphPad Prism. Statistical tests are indicated in each figure legend. Numbers in parentheses in figures indicate non-significant *P*-values. Bar plots show mean ± standard deviation. In box plots, horizontal lines indicate the median and 25th and 75th quantiles; whiskers extend 1.5× the interquartile range from the 25th and 75th percentiles; dots represent possible outliers.

3. Results

3.1 RYR2 is essential for cardiomyocyte maturation

The workflow of the CASAAV technique is shown in *Figure 1A*. Briefly, AAV9 was used to deliver single-guide RNAs (sgRNAs) and Cre recombinase specifically to $Rosa^{fsCas9GFP}$ cardiomyocytes in mice by the cardiomyocyte-specific cTNT promoter. Cre activated Cas9 and GFP expression from $Rosa^{fsCas9GFP}$ and enabled CRISPR/Cas9-mediated KO of the gene of interest.

To achieve CASAAV-based RYR2 depletion, we designed sgRNAs targeting the second exon of *Ryr2* (*Figure 1B*). We previously demonstrated that CASAAV with these sgRNAs efficiently depleted RYR2.[14] We used Cas-OFFinder[34,35] to assess the off-target effects and identified no genomic loci with 0–1 base-pair mismatches relative to these sgRNA sequences. Among the genomic regions showing 2–3 mismatches, only four loci were exonic and their gene expression was not altered upon CASAAV treatment (see Supplementary material online, *Table S1*). Thus, the off-target effects of these sgRNAs were low and unlikely to skew the following analysis.

To rule out the expression of truncated RYR2 proteins, we injected high-dose (3.6×10^9 vg/g) AAV-sgRNA[*Ryr2*]-cTNT-Cre (AAV-sgRNA[*Ryr2*]; KO) or AAV-cTNT-Cre (AAV-Cre; control) into Post-natal Day 1 (P1) mice and collected ventricular tissues at P7 for western blot analysis. The full-length RYR2 protein bands were clearly diminished in the KO group while no smaller bands were increased (see Supplementary material online, *Figure S1A*). Immunofluorescent staining revealed RYR2 loss in over 70% AAV-sgRNA[*Ryr2*]-transduced cardiomyocytes, using GFP as an AAV transduction marker (see Supplementary material online, *Figure S1B*). Calcium transients and cell contractility were fully abolished in KO cardiomyocytes as expected, confirming the essential role of RYR2 in cardiomyocyte excitation–contraction coupling (see Supplementary material online, *Figure 1C and D*).

High-dose AAV-sgRNA[*Ryr2*] transduced ∼72% ventricular cardiomyocytes at P7 (*Figure 1C*). This treatment resulted in death within 2 weeks after birth (*Figure 1D*), decreased cardiac fractional shortening (*Figure 1E*), and prolonged QT interval (see Supplementary material online, *Figure S1E*) at P10. We next titrated the AAV dosage to create genetic mosaic RYR2 depletion in the heart and identified a low dose (3.6×10^8 vg/g) that only transduced ∼16% cardiomyocytes (*Figure 1C*). This dose circumvented animal death and cardiac dysfunction (*Figure 1D and E*), opening the door to study the cell-autonomous function of RYR2 in cardiomyocyte maturation.

We first analyzed the role of RYR2 in T-tubule formation, which is an ultrastructural hallmark of cardiomyocyte maturation that occurs in mice at the 2–3 weeks after birth. *In situ* confocal imaging of the 4-week mosaic hearts revealed a drastic loss of T-tubules in GFP-positive cardiomyocytes (*Figure 1F and G*). This result was further validated by immunostaining of the T-tubule marker CAV3 (caveolin-3) (*Figure 1H*). We also observed disrupted organization of sarcomere Z-lines and reduced distance between adjacent Z-lines (*Figure 1I and J*) in RYR2-depleted cardiomyocytes. These mutant cardiomyocytes had reduced projected cell area, length, and width (*Figure 1K*). Together, these phenotypes indicated that RYR2 is essential for morphological cardiomyocyte maturation.

We next purified 4-week-old GFP-positive cardiomyocytes by FACS, and adopted a published, customized protocol to profile the transcriptomes (FACS-RNA-Seq, *Figure 2A*).[16,36] Principle component analysis (PCA) clearly separated Ctrl and *Ryr2* KO RNA-Seq data (see Supplementary material online, *Figure S2A*). More than 3200 genes were up- or down-regulated by RYR2 depletion (*Figure 2B* and see Supplementary material online, *Table S2*). Myofibrillar isoform switching from *Myh7* and *Tnni1* to *Myh6* and *Tnni3*, which are established markers for cardiomyocyte maturation in mice,[2] was impaired in *Ryr2* KO cells (*Figure 2C*). GSEA using either hallmark (*Figure 2D*)[37] or GO gene sets (see Supplementary material online, *Figure S2B*) showed that RYR2 depletion triggered drastic down-regulation of genes involved in oxidative phosphorylation and fatty acid metabolism.

To further assess cardiomyocyte maturation at the transcriptome level, we took advantage of a published RNA expression profile of P6 and P30 cardiomyocytes.[30] In RYR2-depleted cardiomyocytes, down-regulated genes were pre-dominantly enriched in P30 cardiomyocytes, while up-regulated genes were significantly enriched in P6 cardiomyocytes (*Figure 2E*). An array of essential myofibrillar, mitochondrial, electrophysiological, and calcium-handling genes in mature cardiomyocytes were also perturbed (*Figure 2F*). Thus, RYR2 is essential for the gene expression changes associated with cardiomyocyte maturation.

3.2 RYR2 depletion activates UPRs

As shown in *Figure 2E* (genes in the red box), RYR2 depletion elevated the expression of some genes that could not be explained by maturation defects. We performed GSEA of these up-regulated genes and found UPR and ER stress as the top up-regulated biological processes (*Figure 3A* and see Supplementary material online, *Figure S2C*). UPR/ER stress pathways comprise three classic branches, namely the EIF2AK3 (PERK)-EIF2A(eIF2α)-ATF4 axis, the ERN1(IRE1)-XBP1 axis, and the ATF6 axis (illustrated in *Figure 3B*).[9,10] We examined these ER stress markers as well as representative downstream genes such as *Ddit3* and *Hspa5* in the RNA-seq data and found all genes up-regulated upon RYR2 depletion (*Figure 3C*). This result was further validated by RT–qPCR (see Supplementary material online, *Figure S2D*).

We next studied whether RYR2 depletion triggered post-transcriptional ER stress mechanisms. RNA-seq reads covering *Xbp1* transcripts demonstrated ER stress-induced spliced *Xbp1* (*Xbp1s*) expression in the RYR2-depleted group (*Figure 3D*). This result was further validated by reverse-transcription PCR and RT–qPCR using

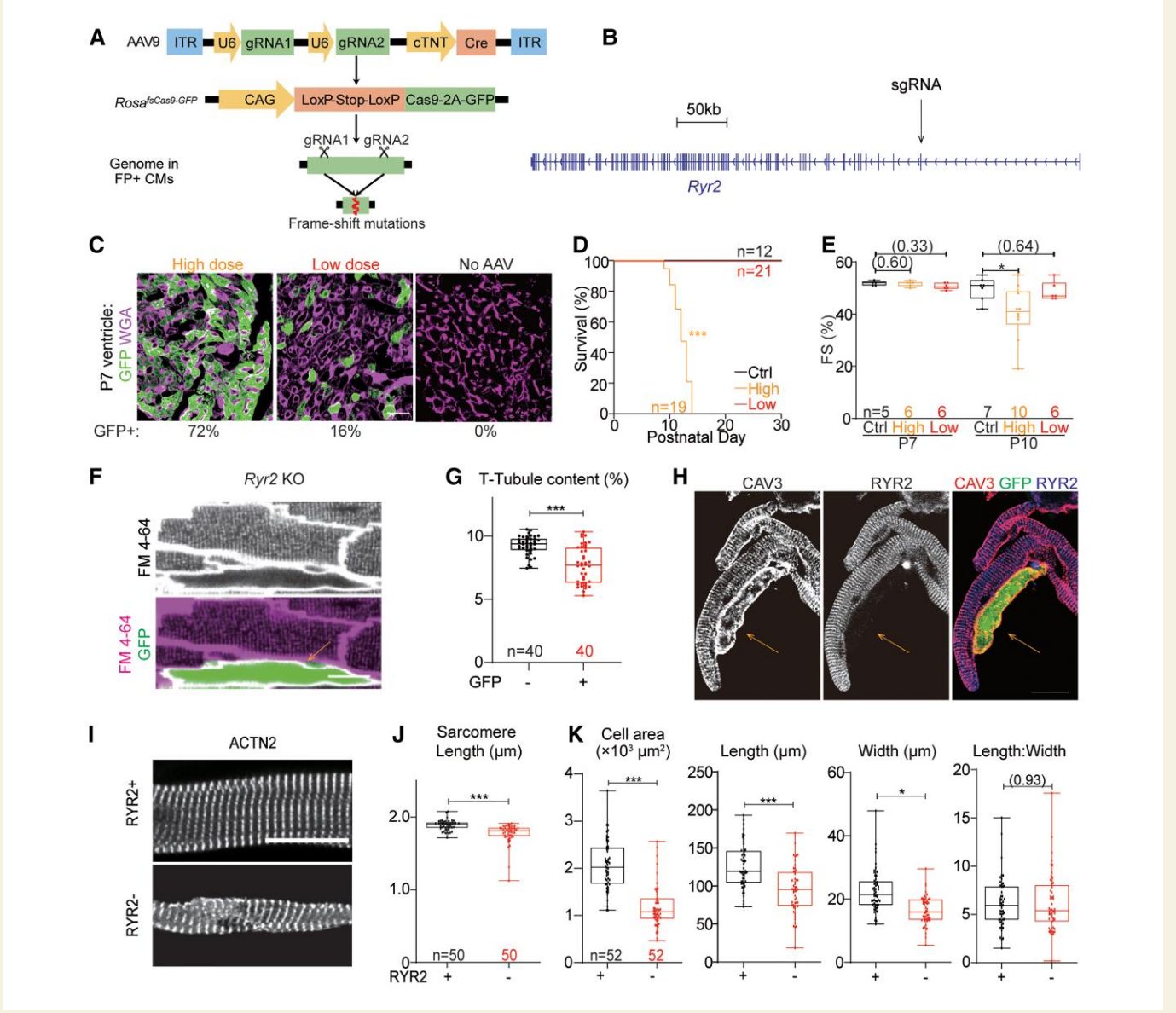

Figure 1 RYR2 depletion perturbs morphological maturation in cardiomyocytes. (*A*) A diagram showing the principle behind CASAAV-based mutagenesis. *Rosa*$^{Cas9GFP/Cas9GFP}$ mice were treated with AAV-sgRNA[*Ryr2*]-cTNT-Cre at P1 to achieve cardiomyocyte-specific RYR2 depletion. (*B*) A diagram showing the gene body of *Ryr2* and the location of sgRNA-targeted regions. (*C*) Fluorescent images of cardiac cryo-sections that were transduced with AAV at high (3.6×10^9 vg/g) and low (3.6×10^8 vg/g) doses, or not transduced with AAV. The fraction of GFP-positive cells was labelled below the images. (*D*) Survival curve. Control (Ctrl) mice were treated with AAV-cTNT-Cre. Log-rank test. (*E*) Fraction shortening measurement by echocardiogram. Unpaired two-tailed *t*-test. In (*D*) and (*E*), *n* indicates animal numbers. (*F*) *In situ* confocal images of myocardium that was perfused with the plasma membrane dye FM 4-64. The arrow indicates a GFP-positive RYR2-depleted cardiomyocyte. (*G*) Quantification of T-tubule contents by AutoTT.[23] (*H*) Immunofluorescent images of isolated cardiomyocytes that were labelled with RYR2 and CAV3 antibodies. The arrow points to a GFP-positive RYR2-negative cardiomyocyte. (*I*) ACTN2 immunofluorescent images of isolated cardiomyocytes. (*J*) Quantification of sarcomere Z-line spacing in isolated cardiomyocytes. (*K*) Quantification of projected cell area, cell length, cell width, and length–width ratio of isolated cardiomyocytes. In (*G*), (*J*), and (*K*), *n* indicates the number of measured cells from two animals and the Mann–Whitney *U* test was performed. In statistical analyses, $*P < 0.05$; $**P < 0.01$; $***P < 0.001$; non-significant *P* values were labelled in parentheses. In fluorescent images, scale bars stand for 20 μm. WGA, wheat germ agglutinin.

primers that specifically detected *Xbp1s* (*Figure 3E*). At the protein level, RYR2 depletion elevated the phosphorylation of EIF2AK3 and EIF2A, enhanced expression of ATF4, XBP1S, the cleaved N-terminal fragments of ATF6 (ATF6N) and HSPA5 (*Figure 3F and G* and see Supplementary material online, *Figure S3*). By comparing the fold changes, the ATF4 protein was more prominently increased than ATF6N and XBP1S (*Figure 3G*).

3.3 ER stress impairs cardiomyocyte maturation

We next sought to determine the impact of ER stress on cardiomyocyte maturation. Tauroursodeoxycholic acid (TUDCA) is an established small molecule that could alleviate ER stress in the heart.[38–41] We applied this drug to mice with mosaic cardiac RYR2 depletion

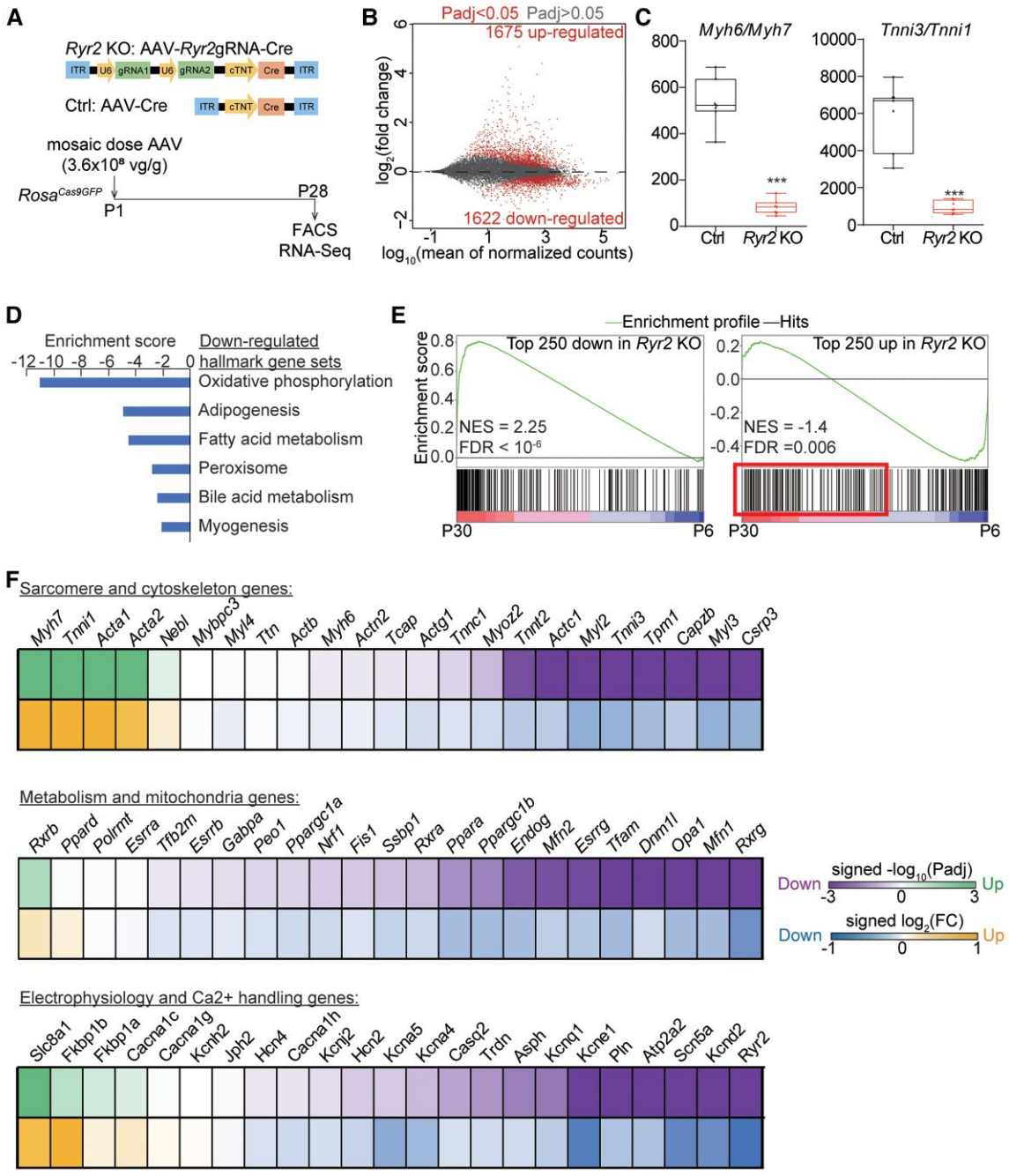

Figure 2 RYR2 depletion perturbs transcriptional maturation in cardiomyocytes. (*A*) RNA-Seq experimental design. Seven biological replicates, one heart per replicate, were analyzed in each group to generate the following data. (*B*) MA plot of genes differentially expressed in RYR2-depleted cardiomyocytes. Each group contained seven replicates. (*C*) Myosin heavy chain and Troponin I isoform switching in RYR2 KO cardiomyocytes. Gene expression values were from RNA-seq data. (*D*) GSEA of the most down-regulated hallmark gene sets upon RYR2 depletion. (*E*) GSEA of enrichment of gene expression changes during cardiomyocyte maturation (P30 vs. P6) for custom gene sets comprising the top 250 genes most up- or down-regulated in Ryr2 knockout. (*F*) Differential expression analysis of key maturation genes upon RYR2 depletion. Up- and down-regulation are presented as positive and negative values, respectively.

(*Figure 4A*) and found that TUDCA significantly mitigated T-tubule defects in RYR2-depleted cardiomyocytes (*Figure 4B and C*).[22] TUDCA also partially rescued defects in cardiomyocyte morphology and sarcomere organization (see Supplementary material online, *Figure S4A and B*). RYR2 was recently implied to influence ER stress through CASQ2,[42] thus we next performed immunofluorescence analysis of CASQ2. We found RYR2 depletion severely perturbed the spatial distribution of CASQ2 in cardiomyocytes and also caused the reduction of CASQ2 level in the heart (see Supplementary material online, *Figure S4C and D*). These data showed that ER stress contributed to cardiomyocyte maturation defects caused by RYR2 depletion.

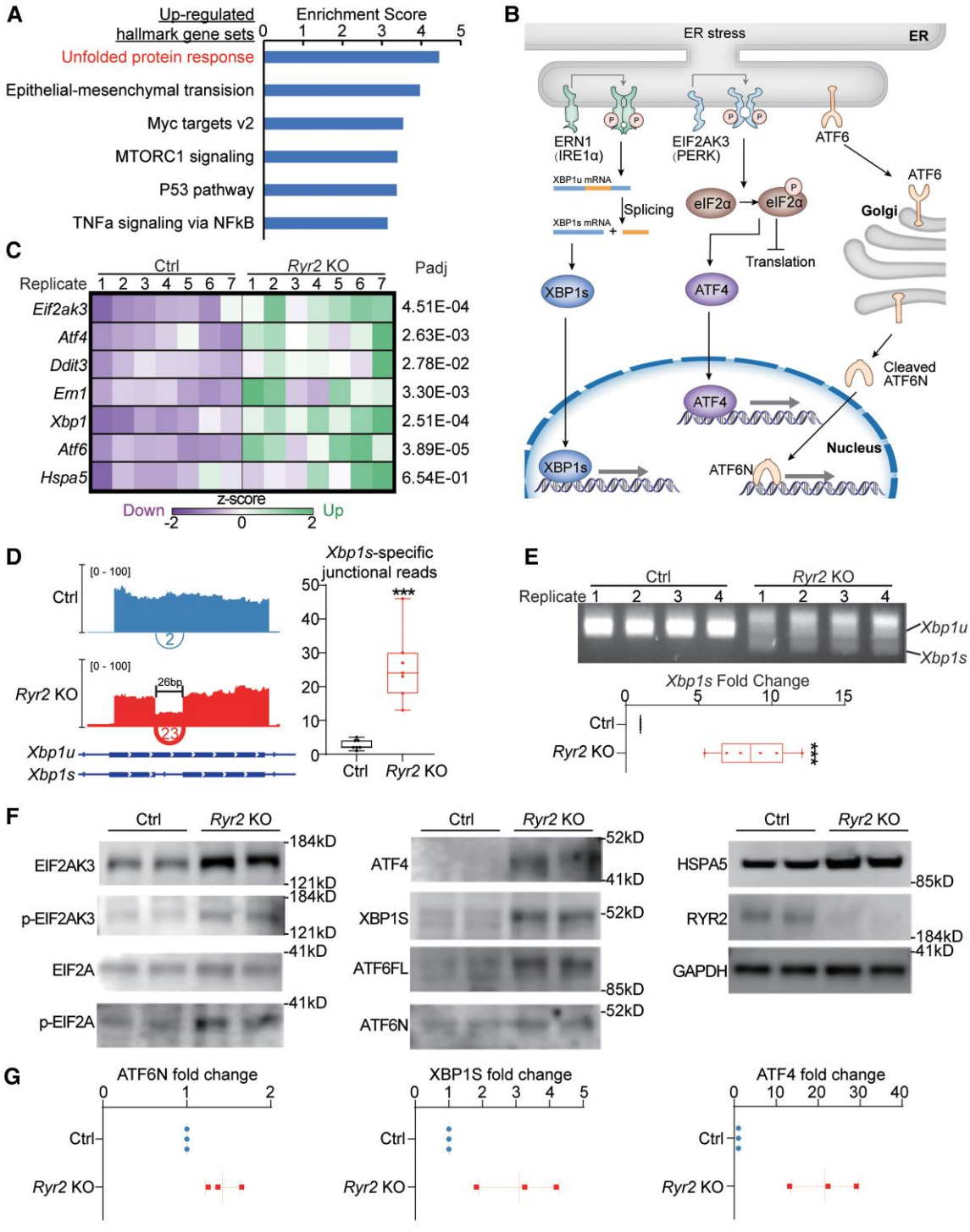

Figure 3 RYR2 depletion triggers unfolded protein responses. (*A*) GSEA of the most up-regulated hallmark gene sets upon RYR2 depletion. (*B*) A diagram of ER stress pathways and key regulatory genes. (*C*) Heatmap of the transcription profiles of key ER stress genes upon RYR2 depletion. (*D*) Sashimi plot of the cryptic splice site in *Xbp1* transcripts as viewed by the Integrative Genome Viewer (left). The number of *Xbp1s*-specific exon junction reads in the RNA-Seq data was plotted (right). Seven biological replicates were analyzed. (*E*) Reverse-transcription PCR analysis of *Xbp1* splicing variants (top). Real-time quantitative PCR analysis of spliced *Xbp1* using isoform-specific primers (bottom). In (*D*) and (*E*), ***$P < 0.001$ by the Mann–Whitney *U* test. (*F*) Western blot analysis of ER stress markers in P10 Ctrl and RYR2-depleted ventricles that were treated with high-dose AAV. (*G*) Quantitative analysis of the western blot results about ATF6N, XBP1S, and ATF4. Three biological replicates were analyzed.

Because ATF4 protein appeared more prominently increased than other ER stress effectors in RYR2-depleted cardiomyocytes (*Figure 3G*), we next generated an AAV vector to overexpress ATF4 specifically in cardiomyocytes (*Figure 4D*) and examined whether ATF4 was sufficient to perturb cardiomyocyte maturation. We first applied high-dose AAV-ATF4 to P1 wildtype pups and analyzed heart

function at P14. We observed significantly decreased fractional shortening and increased left ventricle internal diameters, indicating impaired contractile function in ATF4-overexpressing hearts (see Supplementary material online, *Figure S5A*). Electrocardiogram did not detect significant electrophysiological abnormalities (see Supplementary material online, *Figure S5B*).

We next applied low-dose AAV-ATF4 for a genetic mosaic analysis and observed at P28 perturbed T-tubule maturation (*Figure 4E and F*), myofibril organization (*Figure 4G*), Z-line spacing (*Figure 4H*), and postnatal cardiomyocyte growth (*Figure 4I*). Functionally, isolated ATF4-overexpressing cardiomyocytes exhibited impaired calcium handling (see Supplementary material online, *Figure S5C*) and sarcomere contractility (see Supplementary material online, *Figure S5D*) capacities. We performed FACS-RNA-Seq (*Figure 5A* and see Supplementary material online, *Table S2*) and found that ATF4 drastically disrupted the transcriptomic profile of maturing cardiomyocytes (*Figure 5B* and see Supplementary material online, *Figure S6A*). GSEA showed that ATF4 significantly up-regulated genes that were enriched in P6 cardiomyocytes, and down-regulated genes enriched in P30 cells (see Supplementary material online, *Figure S6B*). Together, these results indicated that ATF4 overexpression was sufficient to perturb cardiomyocyte maturation.

To further determine whether the defects in RYR2-depleted and ATF4-overexpressing cardiomyocytes were relevant, we next performed RTqPCR and found that *Atf4* expression in ATF4-overexpressing cardiomyocytes were only slightly higher (~2-fold) than that in RYR2-depleted cardiomyocytes (see Supplementary material online, *Figure S6C*). We identified differentially expressed genes in both ATF4 overexpression and RYR2 KO experiments and we found their expression fold changes were robustly correlated ($r = 0.91$, *Figure 5C*). GSEA showed that the top up-regulated and down-regulated hallmark gene sets were identical in ATF4 overexpression and RYR2 depletion experiments (*Figure 5D*). Top dysregulated genes in ATF4 overexpressing cardiomyocytes were also enriched in differentially expressed genes in RYR2-depleted cells (*Figure 5E*). These genes include key regulators of myofibrils, mitochondria, electrophysiology, and calcium handling (*Figure 5F*). These data strongly indicated that ATF4 at least partly mediated the impact of RYR2 depletion on cardiomyocyte maturation.

Because the *Xbp1* and *Atf6* axes were also activated in *Ryr2* KO cardiomyocytes, we next produced AAVs to overexpress XBP1S or ATF6N specifically in cardiomyocytes to analyze the effect on cardiomyocyte maturation (see Supplementary material online, *Figure S7A*). Immunofluorescence validated the nuclear localization of these overexpressed proteins (see Supplementary material online, *Figure S7B*). RTqPCR showed that the AAV-mediated overexpression was slightly higher (~3-fold) than the up-regulation in RYR2-depleted cardiomyocytes (see Supplementary material online, *Figure S7C*). *In situ* myocardium imaging showed that the *Xbp1s*- and *Atf6n*-overexpressing cardiomyocytes both exhibited severe defects in T-tubule and cell morphology (see Supplementary material online, *Figure S7D*).

FACS-RNA-Seq was next formed to study the impact of XBP1S and ATF6N on transcription (see Supplementary material online, *Figure S8A* and *Table S2*). PCA clearly separated control, XBP1S overexpression, and ATF6N overexpression data (see Supplementary material online, *Figure S8B*). Overexpression of *Xbp1* and *Atf6* was validated in the RNA-Seq results (see Supplementary material online, *Figure S8C*). Defective isoform switching in *Tnni* and *Myl* genes was validated by the RNA-Seq results in the overexpression groups (see Supplementary material online, *Figure S8D*). GSEA showed that both XBP1S and ATF6N significantly up-regulated genes that were enriched in P6 cardiomyocytes, and down-regulated genes enriched in P30 cells (see Supplementary material online, *Figure S8E*). Collectively, these data showed that XBP1S and ATF6N activation were also able to impair cardiomyocyte maturation.

To further determine the relative contribution of each ER stress pathway to the maturation defects in RYR2-depleted cardiomyocytes, we performed GSEA and found the differentially expressed genes in the XBP1S and ATF6N overexpression samples were significantly enriched in the differentially expressed genes in RYR2-depleted cardiomyocytes (see Supplementary material online, *Figure S9A*). The shared differentially expressed genes in the XBP1S and ATF6N overexpression experiments and RYR2 KO experiments were correlated (see Supplementary material online, *Figure S9B*), but the correlation coefficients were smaller than that observed between ATF4 overexpression and RYR2 KO (comparing *Figure 5C* and see Supplementary material online, *Figure S9B*). Thus, XBP1S and ATF6N likely contributed to the RYR2 KO phenotypes, although to a lesser extent than ATF4.

3.4 ATF4 triggers excessive expression of protein translation machinery components

Because ATF4 was widely reported to activate the pro-apoptotic transcription factor DDIT3 (also known as CHOP),[43–45] we wondered if apoptosis contributed to the maturation defects that we observed after RYR2 depletion or ATF4 overexpression. GSEA showed that ER stress-induced apoptosis genes were up-regulated in both ATF4 overexpression and RYR2 KO RNA-Seq data (see Supplementary material online, *Figure S10*). Among these genes, we validated that *Bcl2*, *Bax* and *Bbc3* (also known as *Puma*) were significantly up-regulated (*Figure 6A* and see Supplementary material online, *Figure S10B*). However, we found that ATF4-overexpressing and RYR2-depleted cardiomyocytes stayed in the myocardium for at least 3 months. No TUNEL-positive cardiomyocytes could be detected with ATF4 overexpression or RYR-depletion (*Figure 6B* and Ssee Supplementary material online, *Figure S10C*). *Bcl2* is anti-apoptotic, so perhaps its up-regulation in ATF4 overexpression or RYR2 depletion (*Figure 6A*) protected cardiomyocytes from apoptosis.

To further rule out the contribution of apoptosis to ATF4- and RYR2-related cardiomyocyte defects, we performed AAV-mediated overexpression of DDIT3 (*Figure 6C*). DDIT3 only mildly perturbed T-tubule maturation (*Figure 6D and E*). FACS-RNA-seq analysis of DDIT3 overexpressing cardiomyocytes showed that <300 genes were changed (see Supplementary material online, *Figures S10D, 6F and Table S2*). Less than half of these genes were perturbed in the ATF4 overexpression experiments (*Figure 6G*). These data showed that ATF4 was unlikely to act through the DDIT3-apoptosis axis.

To explore the mechanism by which ATF4 disrupted cardiomyocyte maturation, we next created AAV vectors that specifically expressed ATF4 fused to a biotin acceptor peptide in cardiomyocytes. Administration of this AAV to mice expressing BirA,[46] which specifically biotinylates the biotin acceptor peptide (*Figure 7A*), facilitated streptavidin pull-down of ATF4 and its bound DNA regions for sequencing analysis. We confirmed by western blots that the ATF4 protein was successfully biotinylated and enriched by streptavidin beads (see Supplementary material online, *Figure S11A*). We performed biotinylation-mediated chromatin immunoprecipitation followed by sequencing (bioChIP-Seq)[30,31] with two biological replicates using input as

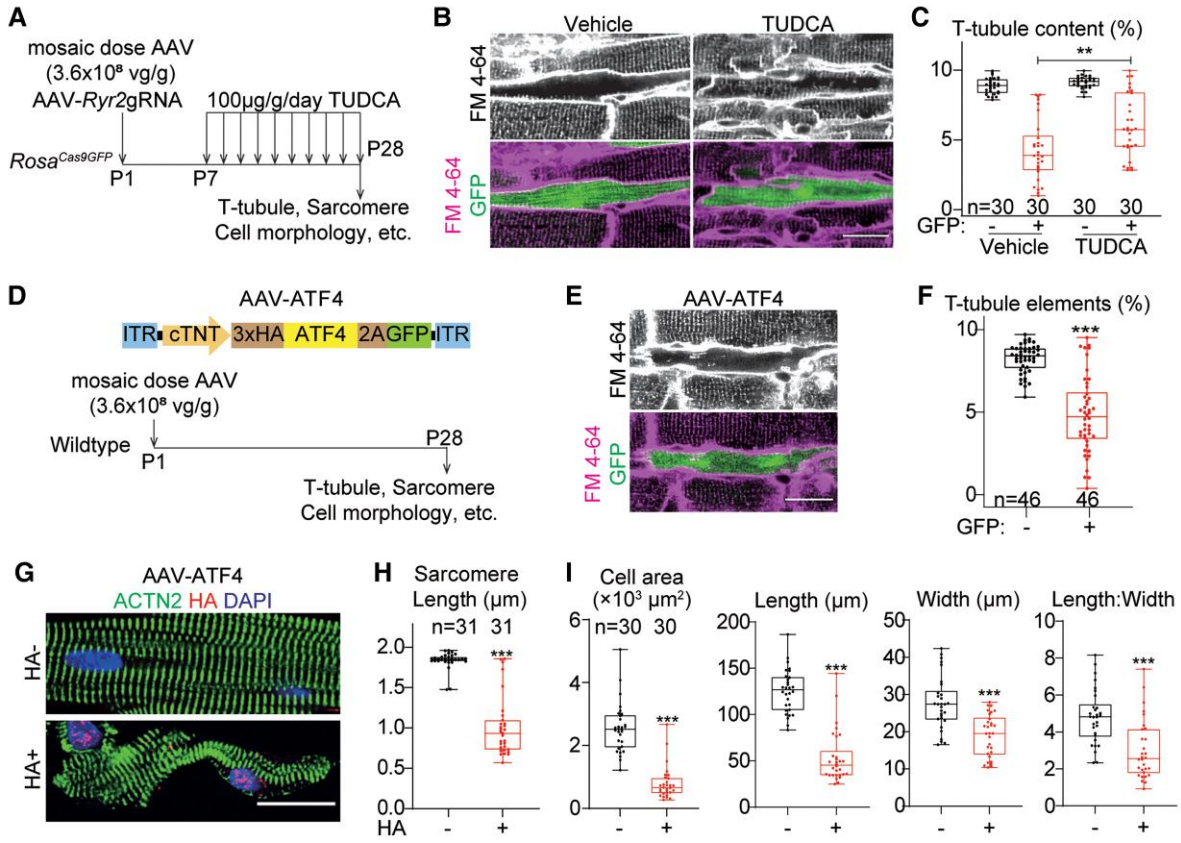

Figure 4 ATF4 overexpression perturbs morphological cardiomyocyte maturation. (*A*) Design of TUDCA treatment experiment in *Rosa*$^{Cas9GFP/Cas9GFP}$ mice. (*B*) *In situ* confocal images of myocardium in the TUDCA experiment. (*C*) Quantification of T-tubule contents by AutoTT. (*D*) Design of the AAV-based ATF4 mosaic overexpression experiment. (*E*) *In situ* confocal images of myocardium in the ATF4 overexpression experiment. GFP-positive cells were overexpressed. (*F*) Quantification of T-tubule contents by AutoTT. (*G*) Immunofluorescent images of isolated cardiomyocytes from AAV-ATF4 treated hearts. HA tag antibody labels ectopic ATF4 expression. (*H*) Quantification of sarcomere Z-line spacing in isolated cardiomyocytes. (*I*) Quantification of projected cell area, cell length, cell width, and length–width ratio of isolated cardiomyocytes. In (*B*), (*E*), and (*G*), scale bars stand for 20 μm. In (*C*), (*F*), (*H*), and (*I*), *n* indicates cardiomyocyte number from two independent hearts and statistical analyses were performed with the Mann–Whitney *U* test. *$P < 0.05$; **$P < 0.01$; ***$P < 0.001$.

controls, and uncovered 62 301 genomic regions bound by ATF4 in cardiomyocytes (*Figure 7B* and see Supplementary material online, *Figure S11B*). These regions covered previously published ATF4-downstream targets such as *Asns* and *Ddit3* (see Supplementary material online, *Figure S11C*),[47] and were enriched with the ATF4 binding motif (see Supplementary material online, *Figure S11D*). Interestingly, several non-ATF4 motifs were also enriched, suggesting that ATF4 indirectly occupied chromatin regions through other transcription factors such as GATA4 and MEF2.[48]

We characterized the genomic features associated with the ATF4-bound regions and found ~21% ATF4-bound sites were proximal to transcription start sites (TSSs) (Fig. 7C). In comparison, only 5.12% (139 847 345 bp/2 730 855 475 bp) genomic regions are proximal to TSSs in the murine genome. Thus, ATF4 exhibited a four-fold enrichment in proximal regions, consistent with a previous publication.[49] Integration of the ATF4 overexpression RNA-Seq data with the bioChIP-Seq data revealed that ATF4 preferentially associated with genes up-regulated by ATF4, indicating that ATF4 is a transcriptional activator. GO analysis showed that the direct downstream genes of ATF4 are involved in tRNA activity, amino acid transport, and protein translation (*Figure 7E*).

Next, we harnessed the ATF4 bioChIP-Seq data to dissect *Ryr2* KO RNA-Seq data. We found about 40% of the up-regulated genes after RYR2 depletion were ATF4 direct downstream targets (*Figure 7F*). Exemplary genes include the immature cardiomyocyte marker *Tnni1* and the classic cardiac stress marker *Nppa* (see Supplementary material online, *Figure S12A and B*). GO term analysis again revealed amino acid biosynthesis pathways as the most relevant biological process (*Figure 7G*), suggesting this pathway contributed to the ATF4-induced maturation defects in *Ryr2* KO cardiomyocytes.

4. Discussion

Cardiomyocyte maturation is an emerging frontier in cardiac developmental biology. Understanding the mechanisms of cardiomyocyte maturation is not only essential to manipulate cardiomyocyte regeneration and the maturity of stem cell-derived cardiomyocytes, but also critical to

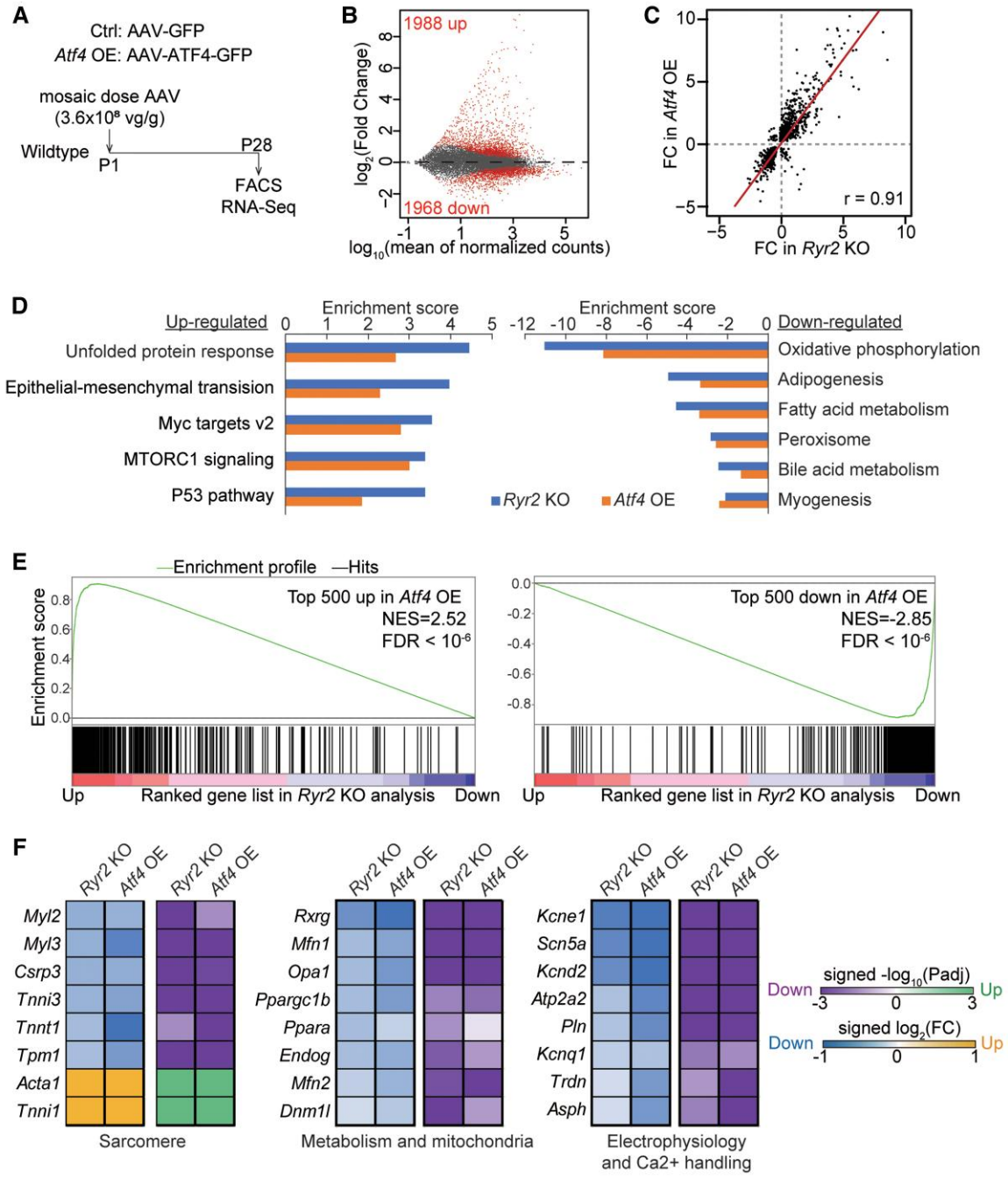

Figure 5 ATF4 overexpression and RYR2 depletion trigger correlated changes in the cardiomyocyte transcriptome. (*A*) RNA-Seq experimental design. Five biological replicates per group were analyzed. (*B*) MA plot of genes differentially regulated in cardiomyocytes by ATF4 overexpression. Genes with $P_{adj} < 0.05$ are highlighted. (*C*) Pearson's correlation analysis of the fold changes of genes differentially expressed in both ATF4 overexpression and RYR2 knockout experiments. (*D*) GSEA of the most differentially regulated hallmark gene sets in ATF4 overexpression and RYR2 depletion experiments. (*E*) GSEA of gene expression changes in Ryr2 KO for enrichment of the genes most up- or down-regulated by ATF4 overexpression. (*F*) Key maturation genes that were similarly dysregulated in ATF4 and RYR2 experiments. Up- and down-regulation are presented as positive and negative values, respectively.

uncover the mechanisms by which maturation defects contribute to heart diseases. Excitation–contraction coupling and calcium handling are critical parameters of cardiomyocyte maturity, but whether calcium contributes to the regulation of cardiomyocyte maturation was unclear. Here, we performed cardiomyocyte-specific and mosaic mutagenesis of RYR2, the major calcium channel that mediates SR/ER calcium release during cardiomyocyte contraction. We found that RYR2 was essential to maintain ER/SR homeostasis, and thereby provided an essential condition for proper cardiomyocyte maturation.

RYR2 is a well-established calcium channel that is essential for the physiological and pathological functions of cardiomyocytes. However, the role of RYR2 in heart development has been difficult to study,

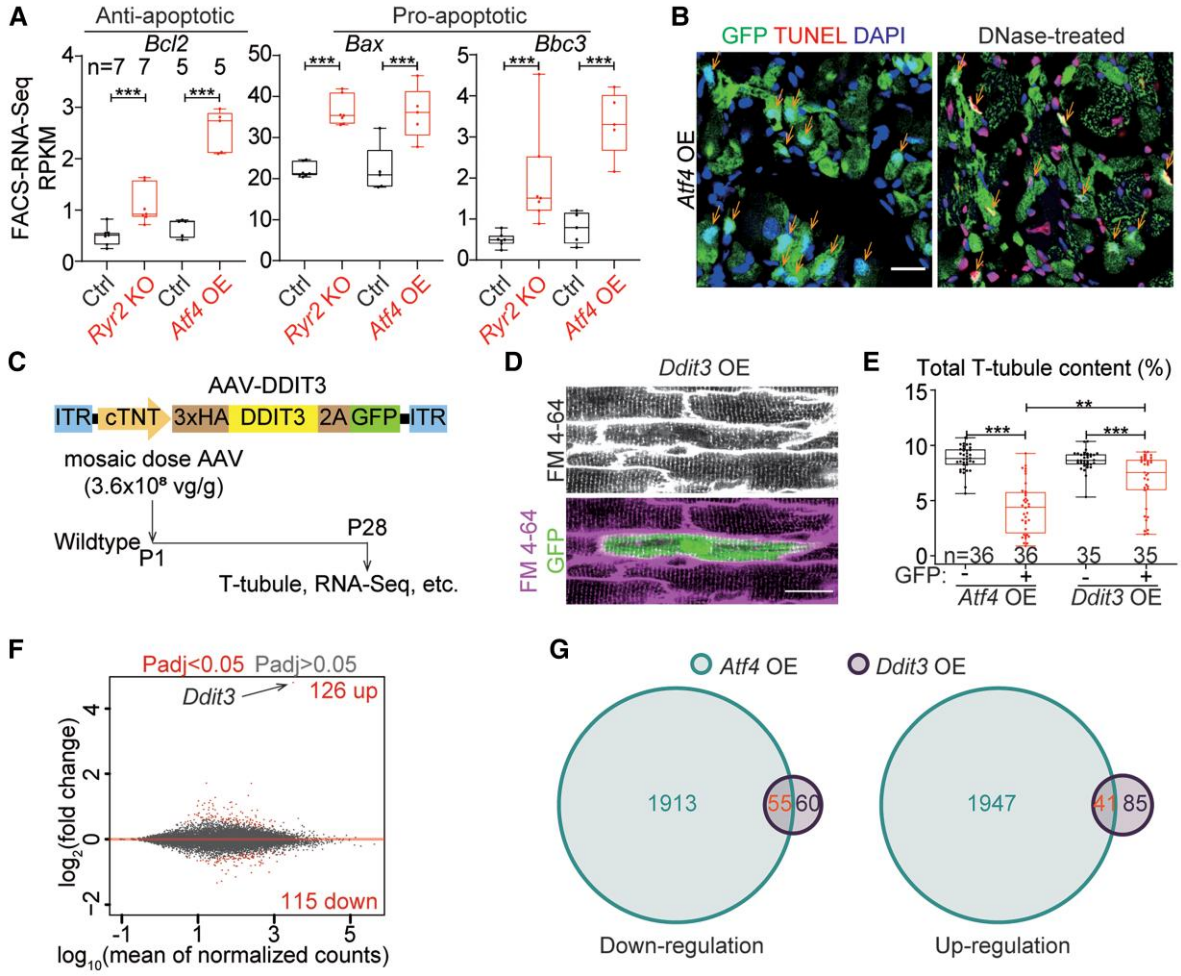

Figure 6 Apoptosis and DDIT3 could not explain the defects in ATF4-overexpressing cardiomyocytes. (*A*) Expression changes of selected apoptosis genes by RNA-seq. *n* indicates the number of independent hearts. (*B*) Fluorescent images of cardiac cryo-sections stained by TUNEL. Arrows point to nuclei in cells that express ATF4-GFP. DNase-treated sections served as a positive control. (*C*) Design of mosaic DDIT3 overexpression experiments. (*D*) In situ confocal images of FM 4-64-labelled myocardium in the mosaic DDIT3 overexpression experiment. (*E*) Quantification of T-tubule content by AutoTT. *n* indicates the number of cardiomyocytes from two hearts. (*F*) MA plot of gene expression in DDIT3 overexpressing cardiomyocytes vs. controls. Highlighted indicates differentially expressed genes (Padj < 0.05). Arrow points to DDIT3, which was the most highly up-regulated gene. (*G*) Venn diagram of the differentially expressed genes in ATF4 and DDIT3 overexpression experiments. The two experiments were performed side-by-side and analyzed using the same pipeline to ensure the two datasets were comparable. In (*B*) and (*D*), scale bars stand for 20 μm. In (*A*) and (*E*), statistical analyses were performed with the Mann–Whitney *U* test. $^{**}P < 0.01$. RPKM, reads per kilobase per million mapped reads.

because conventional genetic ablation of RYR2 lead to acute foetal lethality in mice.[12] Whole-heart cardiomyocyte-specific RYR2 depletion also deposited secondary effects of cardiac dysfunction,[50] which confounded the analysis of cell-autonomous functions of RYR2 in the heart. In this study, we performed genetic mosaic analysis of cardiomyocytes depleted of RYR2 and overcame the technical barriers in the previous animal models. We found new roles of RYR2 in modulating ultrastructural, transcriptional, and functional aspects of cardiomyocyte maturation as well as the elevation of ER stress. This study highlights the importance of performing genetic mosaic analysis to precisely define gene functions in the heart.

ER stress is a double-edged sword in cells. While brief or moderate activation of ER stress pathways is often protective, prolonged, or excessive activation of ER stress causes cell damage or even triggers programmed cell death. A number of studies have revealed the cardiac protective functions of ER stress effectors, such as XBP1S[51,52] and ATF6N.[53,54] However, these studies often focused on adult hearts, and the impact of ER stress on heart development has been understudied. Here, we performed AAV-mediated, acute activation of all three ER stress effectors and observed drastic changes to maturating cardiomyocytes. These experiments were performed in cardiac genetic mosaics, indicating that the damaging effect of ER stress pathways to cardiomyocyte maturation is cell-autonomous and not due to secondary effects caused by cardiac dysfunction and remodelling.

In ER stress, ATF4 is believed to activate DDIT3-mediated apoptosis. In our studies, although ATF4 overexpression drastically impaired cardiomyocyte maturation, we detected minimal cell apoptosis. AAV-mediated overexpression of DDIT3 was also insufficient to trigger cellular apoptosis or defects similar to ATF4 overexpression. These results indicate that DDIT3 is not a major effector of ATF4 in the

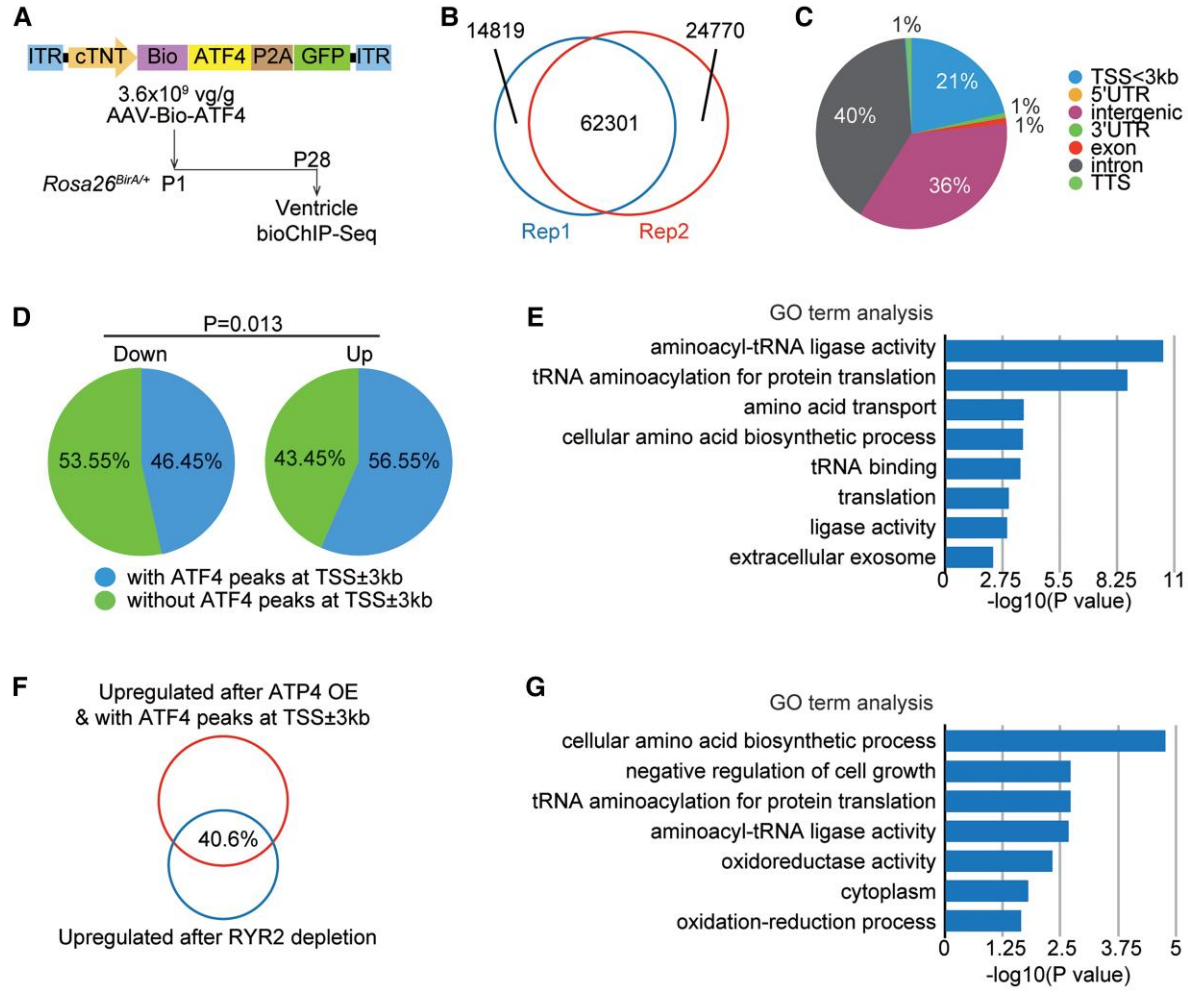

Figure 7 ATF4 directly activates genes that mediate protein translation. (*A*) Design of ATF4 bioChIP-Seq. (*B*) Overlap of ATF4 bound regions in two biologically replicated bioChIP-Seq experiments. A total of 3–4 hearts were collected for each replicate. (*C*) Spatial distribution of ATF4 bound regions in the genome. (*D*) Analysis of ATF4-induced differentially expressed genes with or without ATF4-bound TSSs. Fisher's exact test. (*E*) GO term analysis of direct ATF4 downstream genes that are up-regulated upon ATF4 overexpression and associated with ATF4-bound TSSs. (*F*) Overlap of direct ATF4 downstream genes with the up-regulated genes in *Ryr2* KO cells. (*G*) GO term analysis of direct ATF4 downstream genes that are up-regulated in *Ryr2* KO cells.

regulation of cardiomyocyte maturation. They also suggest that prior data supporting the pro-apoptotic role of DDIT3 reflect non-cell autonomous factors in the context of whole-heart disorders.[43]

Because ATF4 overexpression triggered more severe defects than DDIT3 overexpression, ATF4 likely performs DDIT3-independent functions in cardiomyocytes. To dissect this mechanism, we integrated RNA-Seq and bioChIP-Seq analysis in ATF4 overexpression and found that tRNA, amino acid, and protein translation-related genes are the major ATF4 downstream targets. This finding was also supported by another study using mouse embryonic fibroblasts.[49] Interestingly, a recent study reported that ATF4 could trigger autophagy-mediated protein degradation and cardiomyocyte atrophy.[55] Together, these data show that ATF4 perturbed cardiomyocyte proteostasis, which is essential for cardiomyocyte maturation.

Although we have successfully depicted the impact of RYR2 depletion and ER stress activation in cardiomyocyte maturation, the mechanistic links between RYR2 and ER stress remain unclear. One potential mechanism might involve altered calcium dynamics, which is essential for ER/SR homeostasis. A robust SR calcium measurement platform compatible with the current genetic mosaic analysis needs to be built to test this hypothesis. Alternatively, RYR2 might directly interact with ER stress regulators on the SR membrane and regulate their functions. A recent study indeed reported connections among RYR2, CASQ2, and IRE1α, which was upstream of the XBP1 axis.[42] Future studies are necessary to test whether RYR2 also interacts and regulates the upstream regulators of ATF4 axis.

Human-induced pluripotent stem cell-derived cardiomyocytes (hiPSC-CMs) are widely used as a cell model to understand the pathogenesis of heart diseases and to test the effect of therapeutic strategies. The immaturity of hiPSC-CMs is a major bottleneck that limits the reliability and accuracy of hiPSC-CMs studies. Under routine monolayer culture conditions, RYR2 expression level and subcellular localization in hiPSC-CMs[56] are known to be distinct from mature cardiomyocytes. Our current study implied that the immature RYR2 expression and localization might be one important factor contributing to the impaired maturity of hiPSC-CMs. Therefore, in future studies, it would be

interesting to test the RYR2-ER stress axis in hiPSC-CMs and determine whether this novel regulatory pathway could be manipulated to enhance the outcome of hiPSC-CM-related studies in cardiac regenerative medicine.

Supplementary material

Supplementary material is available at *Cardiovascular Research* online.

Authors' Contributions

Y.G. conceived and conducted the research; W.T.P. provided overall supervision; Y.C., B.D.J., and J.L. performed major experiments; X.Z. and Z.C. analyzed sequencing data; P.Z. conducted bioChIP-seq experiment; N.M., M.Z., and E.D. provided technical support and data analysis; S.G. and F.L. performed calcium analysis; Y.-W.L. and D.-Z.W. helped with analysis of *Xbp1* splicing; Q.M. conducted echocardiography and managed the animal; Y.G. and W.T.P. wrote the manuscript; Y.Z. assisted in manuscript preparation and graphical illustration.

Acknowledgements

We thank PackGene Biotech for assistance in AAV production. We appreciate the technical support from the Dana-Farber Flow Cytometry Core, the HMS Biopolymers Facility, and the animal facilities at Boston Children's Hospital and Peking University Health Science Center.

Ethics Statement

All animal strains and procedures were approved by the Institutional Animal Care and Use Committee of Boston Children's Hospital and Peking University Health Science Center.

Conflict of interest: None declared.

Funding

W.T.P. was supported by the National Institute of Health (R01HL146634 and UM1HL098166) and charitable support from the Boston Children's Hospital Department of Cardiology. Y.G. was supported by the National Natural Science Foundation of China (32100660 and 82170367) and the Beijing Nova Program (Z211100002121003). S.G. was funded by Conselho Nacional de Desenvolvimento Científico e Tecnológico (CNPq) Universal (423465/2018-0) e Fundação de Amparo à Pesquisa do Estado de Minas Gerais (FAPEMIG) Universal (APQ-01510-17). M.Z. was supported by the Postdoctoral Science Foundation of China (2020M680261) and the National Postdoctoral Program for Innovative Talents (BX20200022). E.D was supported by the Natural Science Foundation of China (82070235, and 92168113), the Research Unit of Medical Science Research Management/Basic and Clinical Research of Metabolic Cardiovascular Diseases, the Chinese Academy of Medical Sciences (2021RU003), and the Beijing Municipal Natural Science Foundation (7191013).

Data availability

Next generation sequencing data have been deposited in the Gene Expression Omnibus (GEO) database under the accession code GSE179944 (ATF4 and DDIT3 overexpression RNA-seq), GSE179948 (Ryr2 knockout RNA-seq), GSE179958 (ATF4 bioChIP-seq), and GSE197965 (XBP1S and ATF6N overexpression RNA-Seq). The differential expression analysis results are also attached to Supplementary material online, *Table S2*. Other data supporting the findings of this study are available upon reasonable request.

References

1. Galdos FX, Guo Y, Paige SL, VanDusen NJ, Wu SM, Pu WT. Cardiac regeneration: lessons from development. *Circ Res* 2017;**120**:941–959.
2. Guo Y, Pu WT. Cardiomyocyte maturation: new phase in development. *Circ Res* 2020;**126**:1086–1106.
3. Karbassi E, Fenix A, Marchiano S, Muraoka N, Nakamura K, Yang X, Murry CE. Cardiomyocyte maturation: advances in knowledge and implications for regenerative medicine. *Nat Rev Cardiol* 2020;**17**:341–359.
4. Landstrom AP, Dobrev D, Wehrens XHT. Calcium signaling and cardiac arrhythmias. *Circ Res* 2017;**120**:1969–1993.
5. McCauley MD, Wehrens XH. Targeting ryanodine receptors for anti-arrhythmic therapy. *Acta Pharmacol Sin* 2011;**32**:749–757.
6. Poláková E, Sobie EA. Alterations in T-tubule and dyad structure in heart disease: challenges and opportunities for computational analyses. *Cardiovasc Res* 2013;**98**:233–239.
7. Sallé L, Brette F. T-tubules: a key structure of cardiac function and dysfunction. *Arch. Mal. Coeur Vaiss* 2007;**100**:225–230.
8. Carreras-Sureda A, Pihan P, Hetz C. Calcium signaling at the endoplasmic reticulum: fine-tuning stress responses. *Cell Calcium* 2007;**70**:24–31.
9. Ron D, Walter P. Signal integration in the endoplasmic reticulum unfolded protein response. *Nat Rev Mol Cell Biol* 2007;**8**:519–529.
10. Minamino T, Kitakaze M. ER stress in cardiovascular disease. *J Mol Cell Cardiol* 2010;**48**:1105–1110.
11. Wang S, Binder P, Fang Q, Wang Z, Xiao W, Liu W, Wang X. Endoplasmic reticulum stress in the heart: insights into mechanisms and drug targets. *Br J Pharmacol* 2018;**175**:1293–1304.
12. Takeshima H, Komazaki S, Hirose K, Nishi M, Noda T, Iino M. Embryonic lethality and abnormal cardiac myocytes in mice lacking ryanodine receptor type 2. *EMBO J* 1998;**17**:3309–3316.
13. Guo Y, Pu WT. Genetic mosaics for greater precision in cardiovascular research. *Circ Res* 2018;**123**:27–29.
14. Guo Y, VanDusen NJ, Zhang L, Gu W, Sethi I, Guatimosim S, Ma Q, Jardin BD, Ai Y, Zhang D, Chen B, Guo A, Yuan GC, Song LS, Pu WT. Analysis of cardiac myocyte maturation using CASAAV, a platform for rapid dissection of cardiac myocyte gene function in vivo. *Circ Res* 2017;**120**:1874–1888.
15. VanDusen NJ, Guo Y, Gu W, Pu WT. CASAAV: a CRISPR-based platform for rapid dissection of gene function in vivo. *Curr Protoc Mol Biol* 2017;**120**:31 11 1–31 11 14.
16. Guo Y, Jardin BD, Zhou P, Sethi I, Akerberg BN, Toepfer CN, Ai Y, Li Y, Ma Q, Guatimosim S, Hu Y, Varuzhanyan G, VanDusen NJ, Zhang D, Chan DC, Yuan GC, Seidman CE, Seidman JG, Pu WT. Hierarchical and stage-specific regulation of murine cardiomyocyte maturation by serum response factor. *Nat Commun* 2018;**9**:3837.
17. Grieger JC, Choi VW, Samulski RJ. Production and characterization of adeno-associated viral vectors. *Nat Protoc* 2006;**1**:1412–1428.
18. Wang S, Guo Y, Pu WT. AAV gene transfer to the heart. *Methods Mol Biol* 2021;**2158**:269–280.
19. Chen B, Zhang C, Guo A, Song LS. In situ single photon confocal imaging of cardiomyocyte T-tubule system from Langendorff-perfused hearts. *Front Physiol* 2015;**6**:134.
20. O'Connell TD, Rodrigo MC, Simpson PC. Isolation and culture of adult mouse cardiac myocytes. *Methods Mol Biol* 2007;**357**:271–296.
21. Guo Y, Kim Y, Shimi T, Goldman RD, Zheng Y. Concentration-dependent lamin assembly and its roles in the localization of other nuclear proteins. *Mol Biol Cell* 2014;**25**:1287–1297.
22. Guo A, Song LS. AutoTT: automated detection and analysis of T-tubule architecture in cardiomyocytes. *Biophys J* 2014;**106**:2729–2736.
23. Picelli S, Bjorklund AK, Faridani OR, Sagasser S, Winberg G, Sandberg R. Smart-seq2 for sensitive full-length transcriptome profiling in single cells. *Nat Methods* 2013;**10**:1096–1098.
24. Dobin A, Davis CA, Schlesinger F, Drenkow J, Zaleski C, Jha S, Batut P, Chaisson M, Gingeras TR. STAR: ultrafast universal RNA-seq aligner. *Bioinformatics* 2013;**29**:15–21.
25. Liao Y, Smyth GK, Shi W. featureCounts: an efficient general purpose program for assigning sequence reads to genomic features. *Bioinformatics* 2014;**30**:923–930.
26. Love MI, Huber W, Anders S. Moderated estimation of fold change and dispersion for RNA-seq data with DESeq2. *Genome Biol* 2014;**15**:550.
27. Subramanian A, Tamayo P, Mootha VK, Mukherjee S, Ebert BL, Gillette MA, Paulovich A, Pomeroy SL, Golub TR, Lander ES, Mesirov JP. Gene set enrichment analysis: a knowledge-based approach for interpreting genome-wide expression profiles. *Proc Natl Acad Sci USA* 2005;**102**:15545–15550.
28. Ramirez F, Ryan DP, Gruning B, Bhardwaj V, Kilpert F, Richter AS, Heyne S, Dundar F, Manke T. deepTools2: a next generation web server for deep-sequencing data analysis. *Nucleic Acids Res* 2016;**44**:W160–W165.
29. Robinson JT, Thorvaldsdottir H, Winckler W, Guttman M, Lander ES, Getz G, Mesirov JP. Integrative genomics viewer. *Nat Biotechnol* 2011;**29**:24–26.

30. He A, Kong SW, Ma Q, Pu WT. Co-occupancy by multiple cardiac transcription factors identifies transcriptional enhancers active in heart. *Proc Natl Acad Sci USA* 2011;**108**:5632–5637.
31. He A, Pu WT. Genome-wide location analysis by pull down of in vivo biotinylated transcription factors. *Curr Protoc Mol Biol* 2010;**Chapter 21**:Unit 21 20.
32. Langmead B, Salzberg SL. Fast gapped-read alignment with Bowtie 2. *Nat Methods* 2012;**9**:357–359.
33. Zhang Y, Liu T, Meyer CA, Eeckhoute J, Johnson DS, Bernstein BE, Nusbaum C, Myers RM, Brown M, Li W, Liu XS. Model-based analysis of ChIP-Seq (MACS). *Genome Biol* 2008;**9**:R137.
34. Bae S, Park J, Kim JS. Cas-OFFinder: a fast and versatile algorithm that searches for potential off-target sites of Cas9 RNA-guided endonucleases. *Bioinformatics* 2014;**30**:1473–1475.
35. Hwang GH, Kim JS, Bae S. Web-based CRISPR toolkits: Cas-OFFinder, cas-designer, and cas-analyzer. *Methods Mol Biol* 2021;**2162**:23–33.
36. Guo Y, Cao Y, Jardin BD, Sethi I, Ma Q, Moghadaszadeh B, Troiano EC, Mazumdar N, Trembley MA, Small EM, Yuan GC, Beggs AH, Pu WT. Sarcomeres regulate murine cardiomyocyte maturation through MRTF-SRF signaling. *Proc Natl Acad Sci USA* 2021;**118**:e2008861118.
37. Liberzon A, Birger C, Thorvaldsdóttir H, Ghandi M, Mesirov JP, Tamayo P. The molecular signatures database (MSigDB) hallmark gene set collection. *Cell Syst* 2015;**1**:417–425.
38. Rivard AL, Steer CJ, Kren BT, Rodrigues CM, Castro RE, Bianco RW, Low WC. Administration of tauroursodeoxycholic acid (TUDCA) reduces apoptosis following myocardial infarction in rat. *Am J Chin Med* 2007;**35**:279–295.
39. Groenendyk J, Lee D, Jung J, Dyck JR, Lopaschuk GD, Agellon LB, Michalak M. Inhibition of the unfolded protein response mechanism prevents cardiac fibrosis. *PLoS One* 2016;**11**:e0159682.
40. Ceylan-Isik AF, Sreejayan N, Ren J. Endoplasmic reticulum chaperon tauroursodeoxycholic acid alleviates obesity-induced myocardial contractile dysfunction. *J Mol Cell Cardiol* 2011;**50**:107–116.
41. Rani S, Sreenivasaiah PK, Kim JO, Lee MY, Kang WS, Kim YS, Ahn Y, Park WJ, Cho C, Kim DH. Tauroursodeoxycholic acid (TUDCA) attenuates pressure overload-induced cardiac remodeling by reducing endoplasmic reticulum stress. *PLoS One* 2017;**12**:e0176071.
42. Wang Q, Groenendyk J, Paskevicius T, Qin W, Kor KC, Liu Y, Hiess F, Knollmann BC, Chen SRW, Tang J, Chen XZ, Agellon LB, Michalak M. Two pools of IRE1alpha in cardiac and skeletal muscle cells. *FASEB J* 2019;**33**:8892–8904.
43. Fu HY, Okada K, Liao Y, Tsukamoto O, Isomura T, Asai M, Sawada T, Okuda K, Asano Y, Sanada S, Asanuma H, Asakura M, Takashima S, Komuro I, Kitakaze M, Minamino T. Ablation of C/EBP homologous protein attenuates endoplasmic reticulum-mediated apoptosis and cardiac dysfunction induced by pressure overload. *Circulation* 2010;**122**:361–369.
44. Marciniak SJ, Yun CY, Oyadomari S, Novoa I, Zhang Y, Jungreis R, Nagata K, Harding HP, Ron D. CHOP induces death by promoting protein synthesis and oxidation in the stressed endoplasmic reticulum. *Genes Dev* 2004;**18**:3066–3077.
45. McCullough KD, Martindale JL, Klotz LO, Aw TY, Holbrook NJ. Gadd153 sensitizes cells to endoplasmic reticulum stress by down-regulating Bcl2 and perturbing the cellular redox state. *Mol Cell Biol* 2001;**21**:1249–1259.
46. Driegen S, Ferreira R, van Zon A, Strouboulis J, Jaegle M, Grosveld F, Philipsen S, Meijer D. A generic tool for biotinylation of tagged proteins in transgenic mice. *Transgenic Res* 2005;**14**:477–482.
47. Gwinn DM, Lee AG, Briones-Martin-Del-Campo M, Conn CS, Simpson DR, Scott AI, Le A, Cowan TM, Ruggero D, Sweet-Cordero EA. Oncogenic KRAS regulates amino acid homeostasis and asparagine biosynthesis via ATF4 and alters sensitivity to L-asparaginase. *Cancer Cell* 2018;**33**:91–107.
48. Akerberg BN, Gu F, VanDusen NJ, Zhang X, Dong R, Li K, Zhang B, Zhou B, Sethi I, Ma Q, Wasson L, Wen T, Liu J, Dong K, Conlon FL, Zhou J, Yuan GC, Zhou P, Pu WT. A reference map of murine cardiac transcription factor chromatin occupancy identifies dynamic and conserved enhancers. *Nat Commun* 2019;**10**:4907.
49. Han J, Back SH, Hur J, Lin YH, Gildersleeve R, Shan J, Yuan CL, Krokowski D, Wang S, Hatzoglou M, Kilberg MS, Sartor MA, Kaufman RJ. ER-stress-induced transcriptional regulation increases protein synthesis leading to cell death. *Nat Cell Biol* 2013;**15**:481–490.
50. Bround MJ, Asghari P, Wambolt RB, Bohunek L, Smits C, Philit M, Kieffer TJ, Lakatta EG, Boheler KR, Moore ED, Allard MF, Johnson JD. Cardiac ryanodine receptors control heart rate and rhythmicity in adult mice. *Cardiovasc Res* 2012;**96**:372–380.
51. Schiattarella GG, Altamirano F, Tong D, French KM, Villalobos E, Kim SY, Luo X, Jiang N, May HI, Wang ZV, Hill TM, Mammen PPA, Huang J, Lee DI, Hahn VS, Sharma K, Kass DA, Lavandero S, Gillette TG, Hill JA. Nitrosative stress drives heart failure with preserved ejection fraction. *Nature* 2019;**568**:351–356.
52. Wang ZV, Deng Y, Gao N, Pedrozo Z, Li DL, Morales CR, Criollo A, Luo X, Tan W, Jiang N, Lehrman MA, Rothermel BA, Lee AH, Lavandero S, Mammen PPA, Ferdous A, Gillette TG, Scherer PE, Hill JA. Spliced X-box binding protein 1 couples the unfolded protein response to hexosamine biosynthetic pathway. *Cell* 2014;**156**:1179–1192.
53. Blackwood EA, Azizi K, Thuerauf DJ, Paxman RJ, Plate L, Kelly JW, Wiseman RL, Glembotski CC. Pharmacologic ATF6 activation confers global protection in widespread disease models by reprograming cellular proteostasis. *Nat Commun* 2019;**10**:187.
54. Jin JK, Blackwood EA, Azizi K, Thuerauf DJ, Fahem AG, Hofmann C, Kaufman RJ, Doroudgar S, Glembotski CC. ATF6 decreases myocardial ischemia/reperfusion damage and links ER stress and oxidative stress signaling pathways in the heart. *Circ Res* 2017;**120**:862–875.
55. Vanhoutte D, Schips TG, Vo A, Grimes KM, Baldwin TA, Brody MJ, Accornero F, Sargent MA, Molkentin JD. Thbs1 induces lethal cardiac atrophy through PERK-ATF4 regulated autophagy. *Nat Commun* 2019;**12**:3928.
56. Ivashchenko CY, Pipes GC, Lozinskaya IM, Lin Z, Xiaoping X, Needle S, Grygielko ET, Hu E, Toomey JR, Lepore JJ, Willette RN. Human-induced pluripotent stem cell-derived cardiomyocytes exhibit temporal changes in phenotype. *Am J Physiol Heart Circ Physiol* 2013;**305**:H913–922.